PAPER

Check for updates

Influence of Mg on the Li ion mobility in Li₄₋₂ₓMgₓP₂S₆†

Sven Neuberger, [ID] Neeshma Mathew, [ID] Sheyi Clement Adediwura [ID] and Jörn Schmedt auf der Günne [ID] *

Aliovalent substitution of Li in salts by Mg can generate Li vacancies and thus in principle improve the ionic conductivity. In fact the influence of substitution on ionic conductivity is far more complex. Here the impact of Mg substitution on Li ion mobility is studied in the example of $Li_4P_2S_6$ by a combination of nuclear magnetic resonance experiments on ^{31}P and ^7Li at variable temperatures, impedance spectroscopy and X-ray powder diffraction to elucidate the relationship with structural changes and the effect on mobility on different length scales. It is found that substituting Li ions with Mg ions in $Li_{4-2x}Mg_xP_2S_6$ with $0 \leq x \leq 0.2$ increases the local Li ion mobility up to a certain concentration at which a phase transition induces a different structural realignment of the $P_2S_6^{4-}$ units. The determined activation energies can be assigned to vacancy hopping processes by comparison with nudged elastic band calculations at the density functional level of theory, which shows not only the possibilities but also limitations of substituting Li with Mg.

Introduction

Lithium-rich non-oxido chalcogenide phosphates have become relevant as electrode materials in Li ion batteries and as separator materials in lithium (ion) batteries[1] due to their high lithium ion conductivities,[2] for example lithium argyrodites Li_6PS_5X (X = Cl, Br, I)[3] or $Li_{10}GeP_2S_{12}$.[4] In order to design a compound with high Li ion conductivity, a compound does not only need to be rich in lithium, but also needs to feature high Li ion mobility in two or more dimensions.[5] There are mainly two mechanisms for Li ion mobility in ceramic electrolytes,[5] which are a vacancy-based and an interstitial site-based ion mobility mechanism. Both mechanisms mainly rely on point defects, such as Frenkel[6] and Schottky defects.[7] The overall Li ion conductivity for a vacancy-based mechanism is related to the product of the vacancy number density and the mobility of the defects, *i.e.* in principle a Li-rich compound with many vacancies should be ideal from this point of view.

One way to increase Li vacancy concentration of a Li salt is aliovalent doping,[8] *i.e.* replacing an atom with one of different valence so that additional defects are produced to compensate for the valence mismatch. Aliovalent substitution of atoms of an anionic sublattice[9,10] has been successful for example for Li argyrodites in which a sulfide S^{2-} is substituted by a halide anion X^-. In sum the substitution of Li^+ and S^{2-} with a halide anion X^- and a vacancy □ produced fast ion conductors $Li_{7-x}\square_xPS_{6-x}X_x$ (X = Cl, Br, I).[3,11] For complex anions aliovalent substitution of atoms of a bigger formal oxidation number has been successfully applied to different sulfidophosphates by replacing the center atom of a complex anion as in $Li_{10}MP_2S_{12}$ (M = Sn, Ge, Si),[4,12,13] *i.e.* substitution of M(ɪᴠ) and Li^+ with M(ᴠ) and a vacancy □. A similar strategy is the substitution of Li^+ by a metal atom with higher valence, including Mg^{2+}, Ca^{2+}, Fe^{2+} or Al^{3+} as shown for Mg^{2+} doped $Li_4Ti_5O_{12}$,[14] $Li_{6-x-2y}Ca_yPS_{5-x}Cl_{1+x}$,[15] $Li_{7-2x}Fe_xPS_6$,[16] or $Li_{5.4}Al_{0.2}PS_5Br$.[17] Besides the increase in mobility it has been observed that phase transitions are influenced as in the case of $Li_{7-2x}Fe_xPS_6$[16] where by partial substitution of Li^+ by Fe^{2+} the high temperature modification of Li_7PS_6 was stabilized.[18]

The test system in this study is lithium hexasulfidohypodiphosphate $Li_4P_2S_6$, for which several crystal structures[19–21] have been published on the basis of X-ray and neutron diffraction data with the motivation to resolve the unsatisfactory disorder of P sites in the initially published structure.[22] While the motifs of the different structures – a chain-like arrangement of the $P_2S_6^{4-}$ group and Li atoms on octahedral sites – are found in all proposed structural models, only the model in the space group $P321$ (Z = 3) explains all experimental data including the presence of minimum three P sites as shown by two-dimensional double-quantum ^{31}P NMR.[21] The structural model suggests a fully ordered unit cell, where Li ion hopping should involve interstitial sites or vacancies. While for the different models which are inconsistent with the NMR findings,

University of Siegen, Faculty IV: School of Science and Technology, Department of Chemistry and Biology, Inorganic materials chemistry and Center of Micro- and Nanochemistry and Engineering (Cμ), Adolf-Reichwein-Straße 2, 57068 Siegen, Germany. E-mail: gunnej@chemie.uni-siegen.de

detailed studies[20,23] including quantum-chemical calculations have been done to provide estimates for activation energies, but this is not the case for the model in $P321$. In the course of finalizing the manuscript we became aware of a single-crystal X-ray study in which the authors succeeded to solve the structure of $Li_4P_2S_6$ from twinned crystals,[24] in the space group $P\bar{3}m1$ ($Z = 3$), which is in full agreement with the ^{31}P NMR results, but reduces the number of crystallographic orbitals for Li from 4 to 2. In terms of the arrangement of the atoms it only shows minor deviations from the structure described in the space group $P321$ ($Z = 3$) to which it is a supergroup, so that both structures converted to the space group $P1$ produce the same results in the quantum-chemical calculations shown below. It is an open question if a phase transition between the two structures exists. For this reason we have based this contribution on the structure described in $P321$, which does not change any of the made conclusions about Li mobility though.

Interestingly several groups have reported electrical conductivity values for $Li_4P_2S_6$ which differ by orders of magnitude in the conductivity values at room temperature ($\sigma_{RT} = 1.6 \times 10^{-10}$ S cm^{-1} and 4.7×10^{-5} S cm^{-1})[20,25] and also the reported activation energies differ significantly ($E_A = 0.29$ eV to 0.48 eV).[19,20] Aliovalent substitution has been tried with magnesium with the compositions $Li_{4-2x}Mg_xP_2S_6$, with $x \geq 1/2$, featuring increased ionic conductivities[26] of up to $\sigma_{RT} \sim 10^{-6}$ S cm^{-1}. For the compositions $Li_{3.33}Mg_{0.33}P_2S_6$ and $Li_{2.66}Mg_{0.66}P_2S_6$ trigonal disordered crystal structures (both space group $P\bar{3}1m$)[26] were derived from powder diffraction data which were based on the initial model of $Li_4P_2S_6$ which has P sites with 50% occupancy. Interestingly the high magnesium content phase shows a layered structure as suggested for $Mg_2P_2S_6$[27] in the space group $C2/m$ meaning that small quantities of Li doped into $Mg_2P_2S_6$ cause a phase transition into a phase in the space group $P\bar{3}1m$. An open question is whether in the phase diagram of $Li_4P_2S_6$ $Mg_2P_2S_6$ phases exist, which in the low-Mg doping regime feature an enhanced Li conductivity because of a suppressed phase transition and whether the expected phase transition has a positive or a negative effect on the Li ion conductivity. Furthermore it makes sense to double-check the structural model of the highly substituted phases $Li_{4-2x}Mg_xP_2S_6$ given that the structure of $Li_4P_2S_6$ in the space group $P321$ was not known at the time.

The purpose of this study is to evaluate which effects aliovalent doping/substitution with Mg can have on sulfidophosphates both in terms of structure and ionic conductivity. As a model system serves the ordered and not highly conductive crystalline substance $Li_4P_2S_6$.

Experimental part

Synthesis

All starting materials were stored inside a glove box (MBraun, Garching, Germany) under an argon atmosphere. All sample preparations were carried out in the same glove box under the same conditions.

Magnesium powder (8.868 mmol, 500.0 mg, Alfa Aesar, 99.9%) was filed off a bar with a rasp and placed in a graphite boat in a gas flow quartz glass apparatus. The magnesium was heated in a tube furnace at 590 °C under a H_2S atmosphere for 17 h to obtain magnesium sulfide MgS.

$Li_{4-2x}Mg_xP_2S_6$ was synthesized according to eqn (1). Red phosphorus (1.115 mmol, 138.1 mg, ACROS Organics, 99.999%), sulfur (1.120 mmol, 287.3 mg, ChemPur, 99.999%), lithium sulfide Li_2S (4.353 mmol, 200.0 mg, Alfa Aesar, 99.9%) and magnesium sulfide MgS were thoroughly ground and mixed in an agate mortar and afterwards placed in a graphitized quartz ampoule (8 mm outer diameter). The ampoule was sealed under vacuum and afterwards heated to 800 °C in a tube furnace for seven days.

$$(4 - 2x)Li_2S + 2x\,MgS + P_4 + S_8 \xrightarrow{\Delta} 2\,Li_{4-2x}Mg_xP_2S_6 \quad (1)$$
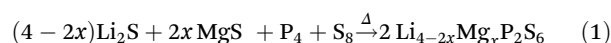
NMR spectroscopy

The chemical shift values of ^{31}P and ^7Li are reported on a deshielding scale, relative to 85% H_3PO_4 and to a solution of LiCl in D_2O (9.7 mol kg^{-1}), respectively. The ^1H resonance of 1% $Si(CH_3)_4$ in $CDCl_3$ served as an external secondary reference using the Ξ values for ^{31}P and ^7Li as reported by the IUPAC[28,29] for all solid-state NMR measurements. All magic angle spinning (MAS) rotors (4 mm, ZrO_2) were packed under an argon atmosphere in a glove box. The ^{31}P and ^7Li MAS NMR measurements were carried out on a Bruker Avance II spectrometer at a frequency of 121.50 MHz and 116.64 MHz, respectively ($B_0 = 7.0$ T), with a home-built 4 mm McKay probe at a sample spinning frequency of $\nu_{rot} = 10$ kHz. For the ^{31}P and ^7Li MAS NMR measurements, a repetition delay of 1 s was used. The static variable temperature (VT) ^7Li NMR measurements were carried out on a Bruker Avance II NMR spectrometer at a frequency of 116.66 MHz ($B_0 = 7.0$ T) with a home-built static McKay probe in an evacuated quartz ampoule ($d = 3$ mm). The analysis and fitting of the spectra were done with Deconv2Dxy (version 0.7).[30] The static ^7Li spectra were deconvoluted with multiple Gaussian functions per spectrum to get a good description of the full lineshape. By using only Gaussian functions for the deconvolution it is straight-forward to determine the second moment of the lineshape.[30]

X-ray powder diffraction

X-ray powder diffraction (XRD) patterns were recorded using a STOE STADI P powder diffractometer (Stoe, Darmstadt, Germany) with Ge(111)-monochromated Cu Kα_1 radiation ($\lambda = 1.54056$ Å) in Debye–Scherrer geometry (capillary inner diameter: 0.48 mm) with a linear position sensitive detector. A 2Θ range between 10° and 90° with a step size of 0.01° was measured, using a counting time of 120 s per step.

Pawley fits and Rietveld analysis

Rietveld refinements were carried out using TOPAS academic V7.1.[31] The $Li_4P_2S_6$ crystal structure[21] with the space group $P321$ (no. 150) was used as a starting model. In the given

order, the following parameters were refined: the scale factor and background coefficients using a Chebyshev function with 10 free parameters, the peak shape using the fundamental parameter approach, the zero-shift error and the lattice constants. For the atom positions of the P atoms, split positions were used to determine site preferences of the respective atoms. The anisotropic displacement parameters were fixed to 1. Mg atoms were not refined due to the lack of scattering contrast. Fit indicators of R_{wp}, R_{exp}, and GOF were used to assess the quality of the refined structural models.[32]

Electrochemical impedance spectroscopy

The $Li_{3.74}Mg_{0.13}P_2S_6$ powder sample was thoroughly ground in an agate mortar and pressed into a cylindrical pellet (diameter $d = 13$ mm) by applying a pressure load of 4 tons (equivalent to $p = 295$ MPa) for 20 minutes. The thickness of the pellet was measured with an electronic micrometer screw gauge. Afterwards, the pellet was brought into contact with silver foil (thickness: 0.1 mm, R. Götze GmbH & Co. KG, silver content 935) by pressing silver sheets (diameter $d = 13$ mm) onto both sides of the pellet (load of 4 tons, equivalent to $p = 295$ MPa for 20 minutes). Samples were handled inside a glove box (MBraun, Garching, Germany) under an argon atmosphere.

Electrochemical impedance spectroscopy (EIS) measurements were performed using an NEISYS electrochemical impedance analyzer (Novocontrol Technologies, Montabaur, Germany). Short and load calibrations were performed before the impedance measurements with a 100 Ω resistor as the load. The prepared pellet was mounted onto a home-made EIS sample cell for impedance measurements. A quasi-four-wire measurement setup in the potentiostatic mode was used, with a perturbation signal of 10 mV amplitude, swept through the 50 mHz to 1 MHz frequency range. The temperature was controlled using variable temperature and flow controller (NMR Service GmbH, Erfurt, Germany) with a constant nitrogen gas flow and a setup with three thermocouples for the sample, the sample holder and the Dewar containing the sample holder. Each temperature point was held for 20 min before every EIS measurement to ensure temperature stability with an accuracy of ±0.1 K throughout the measurement period. The data analysis was performed using home developed software using SciPy libraries[33] which implement non-linear least squares fitting and error analysis.

Computational methods

A plane wave (PW) pseudopotential (PP) method based on density functional theory (DFT) using Quantum Espresso 6.8 (QE)[34] was employed to calculate the Li-ion diffusion properties in $Li_4P_2S_6$.

The cif file of $Li_4P_2S_6$ with the space group $P321$ (ICSD-434755)[21] was converted into an input file using cif2cell 2.0.0[35] for the QE calculations. All fractional co-ordinates were allowed to relax using the QE relax calculations under the periodic boundary conditions. Optimised pseudopotentials of GBRV type[36] were used for the simulations with Monkhorst–Pack scheme[37] based optimisation for the selection of auto-

matic k points. For the final simulations a k-mesh of $4 \times 4 \times 4$ over the Brillouin zone, resulting in 36 k-points including the gamma point, was employed with an error of convergence of 0.001 eV. A plane wave kinetic energy cut-off of 60 eV and kinetic energy cut-off for charge density of 525 eV were used with an error of convergence of 0.027 eV.[38]

Climbing Image-Nudged Elastic Band (CI-NEB)[39] calculations were performed to calculate the activation energy for the supercell containing a $1 \times 1 \times 2$ unit cell.[40] The Li-ion diffusion was calculated by creating vacancies in the nearest sites as the first and last images. Eight intermediate images were used along with the first and last images to identify the diffusion pathway for the Li-ion transport.[41]

Results and discussion

In order to obtain a better understanding of the effect of Mg doping, in the first part the structural impact is studied by X-ray diffraction and ^{31}P magic-angle-spinning (MAS) NMR and in the second part the impact on Li mobility is studied by ^{7}Li NMR, nudged elastic band calculations and impedance spectroscopy (EIS). Finally, the results are discussed in the context with earlier work on this system and their implications on Mg doping in general.

Investigation of structural changes

What is apparent from the previous studies is that the limiting phases in the phase diagram *i.e.* $Mg_2P_2S_6$ in the space group $C2/m$ [27] and $Li_4P_2S_6$ in the space group $P\bar{3}m1$ or $P321$[21] do not share a structure which allows the formation of a single solid solution over the complete range because the P_2S_6 groups do not have a compatible arrangement relative to each other. What could be shown convincingly in the previous study[26] is that even a small amount of substitution of Mg for Li causes a phase transition away from the monoclinic structure of $Mg_2P_2S_6$. For this reason, the focus here is on the low-substitution regime. Important for the solution of the structure of $Li_4P_2S_6$ in the space group $P321$ were three ^{31}P NMR peaks which could be resolved by 2D ^{31}P single-quantum double-quantum correlation NMR experiments. Besides, the structural models need to explain a reflection in the powder diffraction at 16.6° [21,24] which was absent in previously suggested models. These markers can thus help to identify a phase transition to a layered structural arrangement of the P_2S_6 groups.

The ^{31}P MAS NMR spectra of $Li_{4-2x}Mg_xP_2S_6$ (Fig. 1) contain two sharp peaks at $\delta = 107.3$ and 109.2 ppm with a peak area ratio of exactly $1.0 : 2.0$ at magnesium contents below $x = 0.07$. With higher magnesium concentrations above $x > 0.07$, the peak area ratio changes and the signals start to merge and become broader indicating higher disorder due to structural changes and defect formation. The ^{31}P MAS NMR spectra over a wider ppm range are depicted in Fig. S1.† Also, the T_1 relaxation times of the ^{31}P NMR signals decrease with increasing magnesium content (Fig. S2†). ^{31}P MAS NMR, scanning electron microscopy coupled with energy dispersive X-ray spectroscopy and X-ray diffraction (Fig. S10–S13†) give evidence of
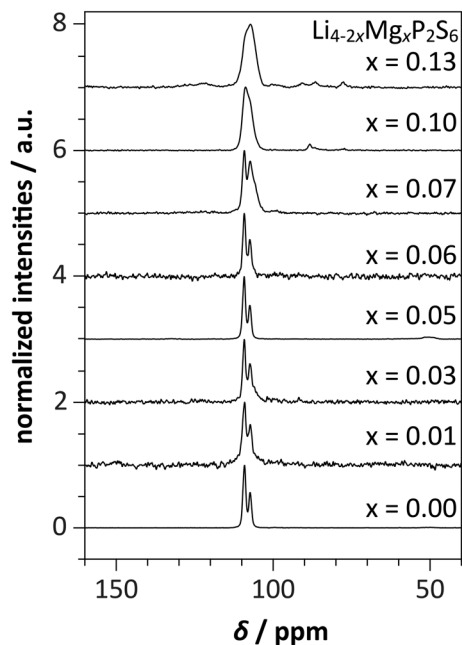
Fig. 1 Experimental ^{31}P MAS NMR spectra of $Li_{4-2x}Mg_xP_2S_6$ at a sample spinning frequency ν_{rot} of 10 kHz. At low Mg content, the ^{31}P MAS NMR spectra contain the characteristic signals of $Li_4P_2S_6$ with a peak area ratio of exactly 1.0 : 2.0, which merge into one broad signal at Mg concentrations of $x > 0.06$.

Fig. 2 (a) X-ray powder diffraction patterns (Cu Kα_1 radiation) of $Li_{4-2x}Mg_xP_2S_6$ with increasing Mg^{2+} content. The position of the most intense diffraction peak of $Li_4P_2S_6$ is marked with a red line. All diffraction patterns only show sharp diffraction peaks of $Li_4P_2S_6$.[21] (b) Detailed comparison of the (101) Miller reflection (at 16.6°) and the (110) Miller reflection (at 16.9°) of $Li_{4-2x}Mg_xP_2S_6$ with increasing Mg^{2+} content. The positions of the two reflections are marked with dashed lines. At higher Mg^{2+} concentrations the intensity of the (101) Miller reflection decreases until it completely vanishes at $x \geq 0.07$.
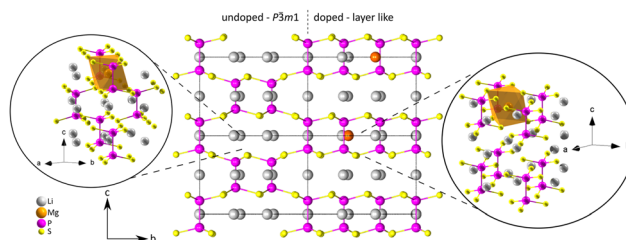
Fig. 3 Visualization of a 2 × 2 × 2 supercell of $Li_{4-2x}Mg_xP_2S_6$. The structural transformation from the space group $P321$ (left cells) to a layered structural model occurs due to an incorporation of Mg^{2+} ions. The doping process leads to a $P\bar{3}1m$ like layered alignment of the $P_2S_6^{4-}$ units similar to that for $Mg_2P_2S_6$ (space group $C2/m$) and as expected for the structural model of $Li_{3.33}Mg_{0.33}P_2S_6$ (space group $P\bar{3}1m$).[26] The insets show the coordination environments for the Mg^{2+} ions (orange) for the different structural models. In the space group $P321$, the coordination polyhedra of Mg^{2+} are slightly distorted due to a different alignment and thus leads to a different number of $P_2S_6^{4-}$ units surrounding the central atom of the polyhedron.

a homogeneous compound and do not give evidence for side-phases.

The broadening of the ^{31}P NMR resonances is expected for a disordered phase where Li atoms are statistically substituted by Mg atoms even without a change of the crystal structure. However, the change in peak area ratio at values of x bigger than 0.07 is indicative of a structural change, *i.e.* a change of the space group and or structure type of $Li_{4-2x}Mg_xP_2S_6$. This can be interpreted as a solubility limit of Mg ($x \approx 0.07$) in the structure of pure $Li_4P_2S_6$. The peak broadening is consistent with the formation of a solid solution and not a mixture of ordered phases.

To further analyze the structural changes, $Li_{4-2x}Mg_xP_2S_6$ was analyzed with X-ray powder diffraction. Up to the highest degree of Mg substitution made in this study of $x = 0.20$, the XRD patterns only show sharp reflections similar to those of $Li_4P_2S_6$[21] (Fig. 2a). However, it should be noted that the 101 reflection at a 2Θ angle of 16.6° disappears at high substitution levels (Fig. 2b). These results confirm the structural model proposed for high substitution levels[26] in the space group $P\bar{3}1m$. Helpful in this context are the previous trials for solving the structure of $Li_4P_2S_6$[19,20,22] which have suggested layered structures and are consistent with the powder diffractogram with a reflection missing at a 2Θ angle of 16.6°. The results confirm the interpretation of Mg-substitution at high levels by Takada *et al.* but require a revision in the low-substitution regime, where up to a composition of $x = 0.07$ a defective structure of $Li_4P_2S_6$ (Fig. 3 left, a model based on $P321$) is
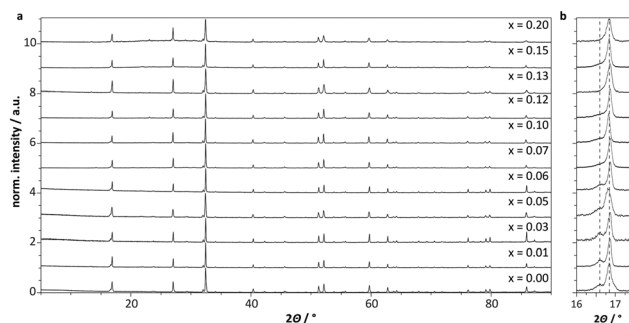
preferred over the layered arrangement (Fig. 3 right, a model based on $P\bar{3}1m$ ($Z = 1$)). The full-scale figure is also depicted in Fig. S3.†

To understand how the substitution process leads to a phase transition, it is helpful to compare the limiting structures. Following the structural models of $Li_{3.33}Mg_{0.33}P_2S_6$ (space group $P\bar{3}1m$)[26] and $Mg_2P_2S_6$ (space group $C2/m$),[42] the preferred positions for the Mg^{2+} ions are the sites within the $P_2S_6^{4-}$ layer (Fig. 3 right) while the defects are located in the interlayer. From the relative arrangement of the P_2S_6 groups it is clear that a solid solution with only gradual changes is impossible.

This interpretation is further corroborated by the results of Rietveld refinements carried out using a structural model with the space group $P321$ and with extra split positions for the P

atoms with variable occupancy in order to trace the structural changes. Due to the lack of scattering contrast only the heavy elements were refined and Mg/Li were not explicitly determined but their atom positions were fixed to the values of the undoped compound with the space group *P*321. The split position in principle allows for a gradual change of the arrangement from the *P*321 structure over to the layered arrangement.

The shift of the P1 atoms upon increasing Mg^{2+} concentration results in an additional crystallographic site P1b shifted by half of the lattice constant in the *z*-direction in contrast to the original P1a site (Fig. 4). The occupancy factor of the P1a site significantly drops at *x* > 0.05, which is in agreement with the suggested model. An exemplary structural model is depicted in Fig. 5 for *x* = 0.13 and Table 1.

Investigation of the Li ion mobility

The questions we wanted to answer are, if in the low Mg substitution regime an increase in Li ion conductivity exists and

Table 1 Exemplary crystallographic data (atomic coordinates, B_{eq}, and occupancy) for the structural model of $Li_{3.74}Mg_{0.13}P_2S_6$ at room temperature, obtained from Rietveld refinements of X-ray powder data (λ = 1.54060 Å) and isotropic displacement parameters without refining the Mg^{2+} ions

$Li_{3.74}Mg_{0.13}P_2S_6$ structure from X-ray powder diffraction (space group *P*321, no. 150);

a = 10. 5211(2) Å; *c* = 6. 59 924 (18) Å

Fit residuals (R_{wp}, R_{exp}, GOF): 10.47, 7.80, 1.34

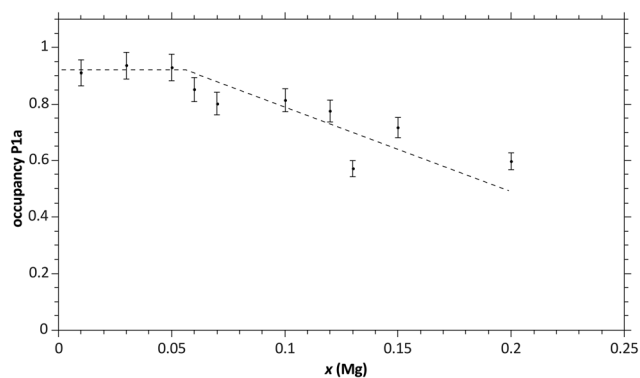| Atom	Wyckoff site	X	Y	z	Occ.	$B_{eq}/Å^2$
Li1	3e	0.625	0	0	0.935	1
Li2	3f	0.631	0	0.5	0.935	1
Li3	3e	0.317	0	0	0.935	1
Li4	3f	0.329	0	0.5	0.935	1
P1a	2c	0	0	0.17	0.571(8)	1
P1b	2c	0	0	0.663	0.429(8)	1
P2	2d	0.333	0.666	0.663	1	1
P3	2d	0.333	0.666	0.335	1	1
S1	6g	0.104(2)	0.211(1)	0.247(1)	1	1
S2	6g	0.114(1)	0.560(2)	0.251(1)	1	1
S3	6g	0.452(2)	0.227(3)	0.254(1)	1	1

Fig. 4 Change of the occupancy factor of the P1a site with increasing Mg^{2+} concentration; the two dashed lines are a guide to the eye. The occupancy factor is close to 1 at concentrations *x* ≤ 0.05. At *x* > 0.05, the occupancy factor decreases, indicating a site preference for the P1b site of the structural model.
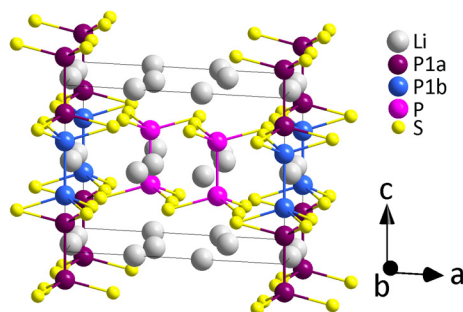

Fig. 5 Exemplary structural model of $Li_{3.74}Mg_{0.13}P_2S_6$ at room temperature, obtained from Rietveld refinements of X-ray powder data (λ = 1.54060 Å) without refining the Mg^{2+} ions. The P1a and P1b sites are indicated with different colors to show the shift of the $P_2S_6^{4-}$ ions upon increasing Mg concentration.

what can be learned about the Li ion motion in the two different structure types. A critical point in the Mg substitution strategy is that while the vacancy concentration increases with increasing Mg content, Mg could act as a "roadblock" in the pathway of the mobile Li ions because of its higher formal charge. To this end ^7Li NMR and nudged elastic-band calculations were utilized to study microscopic Li mobility and electrochemical impedance spectroscopy (EIS) to study macroscopic Li mobility.

In such a case, moment analysis provides a handy tool for motion analysis.[43–45] The decrease of the second moments M_2 of the central transition of the static ^7Li signals is indicative of motional narrowing and hence of motional averaging of the anisotropic terms of the chemical shift tensor. For the static ^7Li NMR signals, the second moments M_2 were calculated to quantify the change in line broadening (Fig. 6a). The static ^7Li NMR signals increase and the room temperature ^7Li T_1 relaxation time shows a change of trend for an *x* value of about 0.07. This is consistent with the postulated phase change at around the same value as observed by ^{31}P MAS NMR and XRD. If the ^7Li quadrupole interaction is assumed to be conserved upon Mg substitution, then the sharper lineshape can be interpreted as a more efficient motional averaging, because of a faster Li mobility. The room temperature ^7Li T_1 relaxation times can be interpreted in a similar manner assuming that the temperature applies to the low-temperature regime of a plot of relaxation rate *versus* inverse temperature rate. In that regime according to BPP theory[46] an increase in relaxation rate $1/T_1$ corresponds to a decrease in the correlation time related to Li mobility, *i.e.* in a crude approximation, a higher relaxation rate is indicative of a higher Li mobility. A consequence of this interpretation is that there is no fast Li conducting phase in the low substitution regime and that the layered
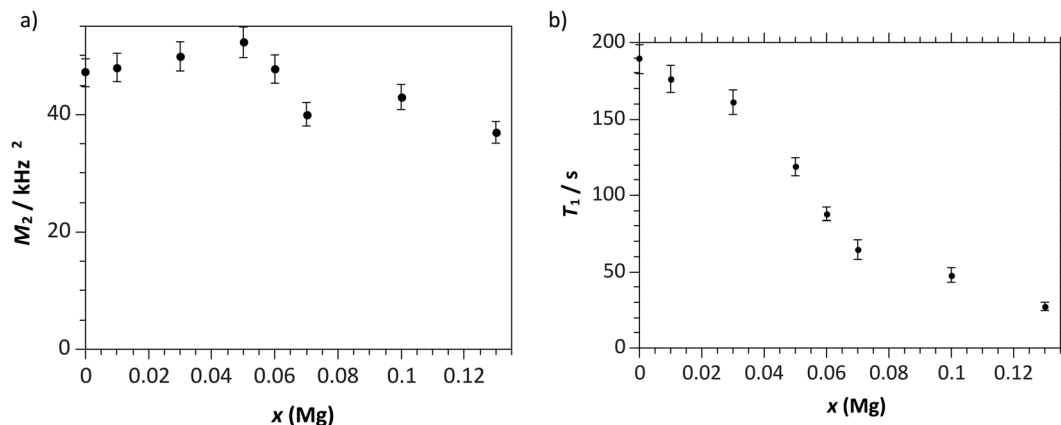
Fig. 6 (a) Second moments M_2 of the static ^{7}Li NMR signals of $Li_{4-2x}Mg_xP_2S_6$. M_2 first increases with increasing Mg^{2+} concentration up to $x = 0.05$. At $x \geq 0.06$, the second moments start to decrease. (b) T_1 relaxation times of the ^{7}Li NMR signals of $Li_{4-2x}Mg_xP_2S_6$ at 116.66 MHz. The T_1 relaxation times decrease with increasing Mg^{2+} concentration. At $x \geq 0.05$, the T_1 relaxation time decreases faster until $x = 0.07$.

structure which is preferred at high substitution levels is beneficial for Li-ion conductivity.

Finally, what remains to be clarified are the activation energies for a vacancy based ion conduction mechanism. For this purpose, detailed studies were done on $Li_{3.74}Mg_{0.13}P_2S_6$ with the help of static ^{7}Li variable temperature (VT) NMR and line shape analysis as well as electrochemical impedance spectroscopy (EIS). In the static ^{7}Li VT NMR spectra (Fig. 7a), a big change in line shape was noticeable due to motional narrowing.

The theory devised by Waugh and Fedin[43,44] can be used to estimate the activation energy for lithium ion motion with an inaccuracy of 10% using the onset temperature T_{onset} of this motional process according to eqn (2). Therefore, the onset points for the motional narrowing for $Li_{3.74}Mg_{0.13}P_2S_6$ and

$Li_4P_2S_6$ were constructed as an intersection of two linear fits $g(T)$ and $h(T)$ (eqn (S1) and (S2)†).

$$E_A = 0.1547 \frac{kJ}{mol \times K} \times T_{onset} \quad (2)$$

Onset temperatures of $T_{onset} = 342.3$ K for $Li_{3.74}Mg_{0.13}P_2S_6$ and $T_{onset} = 380.6$ K for $Li_4P_2S_6$ were determined, which correspond to activation energies E_A of 0.55(5) eV for $Li_{3.74}Mg_{0.13}P_2S_6$ and 0.62(6) eV for $Li_4P_2S_6$, respectively, *i.e.* a small reduction of the activation energy is observed which describes the local Li ion mobility.

Macroscopic motion was studied by EIS in $Li_4P_2S_6$ which was required because pure $Li_4P_2S_6$ did not get characterized together with the Mg substituted compounds.[26] The Nyquist plots of both the pure and the Mg substituted compound
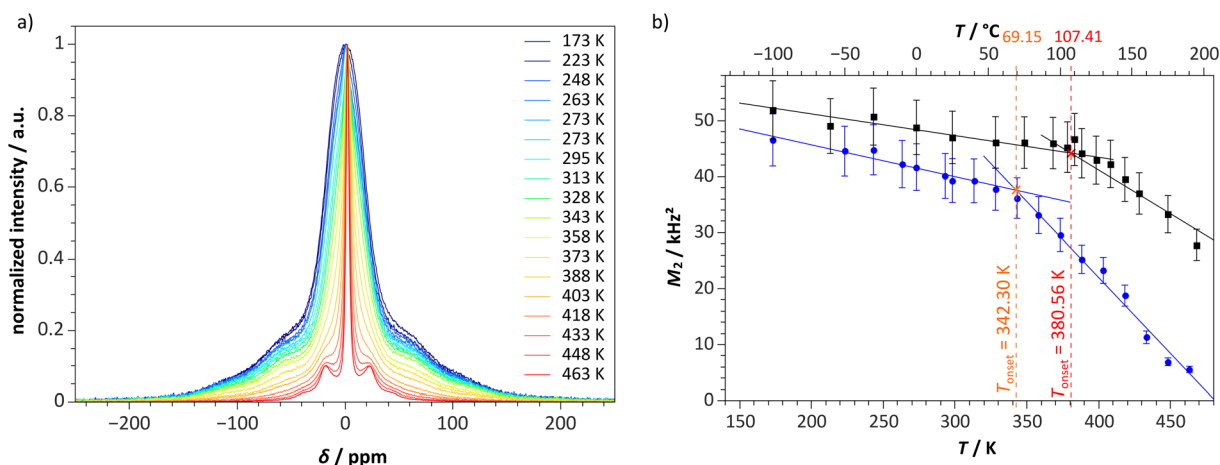

Fig. 7 (a) Normalized static ^{7}Li VT NMR spectra of $Li_{3.74}Mg_{0.13}P_2S_6$ from 173 K (dark blue) to 463 K (red). The static ^{7}Li NMR signals become sharper with increasing temperature. (b) Second moments M_2 of the static ^{7}Li VT NMR signals of $Li_{3.74}Mg_{0.13}P_2S_6$ (blue points) and $Li_4P_2S_6$ (black squares) with two fitted lines each. The intersections of two lines for each mark the onset points at the temperature at which the motional narrowing becomes more intense.

Paper

$Li_{3.74}Mg_{0.13}P_2S_6$ (Fig. 8) show only one large resistive contribution to the impedance data, depicting the bulk region based on the effective capacitances obtained from the equivalent circuit analysis (Table 2). To ensure reproducibility of the electrochemical impedance spectroscopy measurements, data from a second heating cycle were also recorded for both compounds, exhibiting the same ionic behavior as the first heating cycle for both compounds. Hence, both compounds did not change during the measurement process (Fig. 9).

The room temperature Li ion conductivity $\sigma_{298\ K}$ of undoped $Li_4P_2S_6$ reported here is lower than the previously reported values.[19,20,25] Also, the activation energy E_A^{EIS} of $Li_4P_2S_6$ is much higher than the ones reported in the litera-

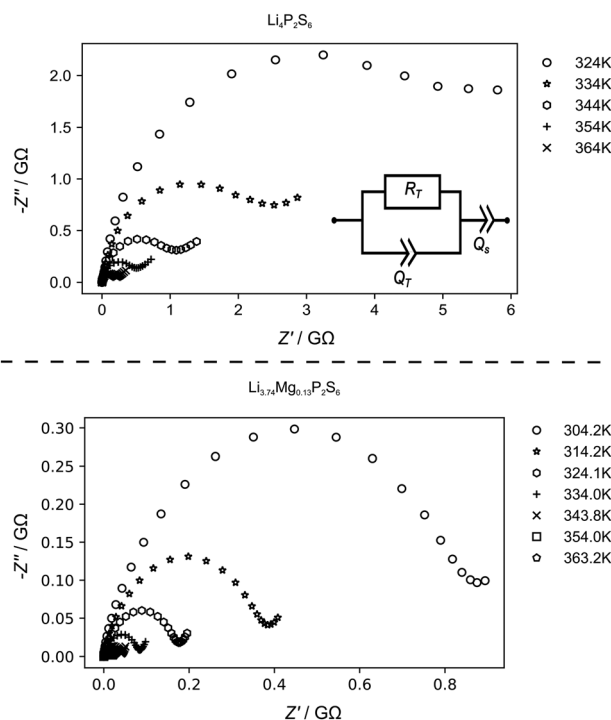**Fig. 9** Arrhenius plot of the logarithmic ion conductivities of $Li_4P_2S_6$ and $Li_{3.74}Mg_{0.13}P_2S_6$ as a function of the reciprocal temperature and the linear fits are indicated with dashed lines. The activation energy for the Li ion motion can be estimated from the slope of a linear fit.

Fig. 8 Nyquist plots of the electrochemical impedance spectroscopy measurements of $Li_4P_2S_6$ and $Li_{3.74}Mg_{0.13}P_2S_6$ measured between 304 K and 364 K. The plot shows one half cycle per temperature. The inset shows the circuit configuration used as a fit model for the Nyquist plots consisting of a resistor R_T, a constant phase element Q_T and a constant phase element for the electrode region Q_s.

ture. Such deviations are not uncommon and a possible explanation for these deviations can be found in the different preparation techniques. The reported ^{31}P NMR spectrum of crystalline $Li_4P_2S_6$ with an ionic conductivity of 1.6×10^{-10} S cm^{-1} shows the presence of side phases of Li_3PO_4 and Li_3PS_4.[20] The reported ionic conductivity of 4.7×10^{-5} S cm^{-1} resulted from powder samples produced by mechanical milling and they show a low degree of crystallinity in the X-ray diffraction patterns.[25] The third reported value of 2.4×10^{-7} S cm^{-1} results from powder samples, which were post processed by a washing step, ball milling and annealing.[19] While it is known that the sample preparation for impedance spectroscopy can lead to significant uncertainty in the conductivity parameter, we ascribe the deviations here mostly to purity, morphology and crystallite sizes of the $Li_4P_2S_6$ powder samples which have been investigated.

The results from the EIS measurements presented here confirm the assumed increase in ionic conductivity (Table 2) by magnesium substitution.[26] Furthermore it is shown that the overall conductivity of pure $Li_4P_2S_6$ is low while the activation energy agrees reasonably well with those found in previous studies[19,20,25] where compounds of good crystallinity and purity were studied i.e. in ref. 20 (Table 2). It can be concluded that the Mg substitution leads to both a phase change and increase of the vacancy concentration which are beneficial for ionic conductivity.

Finally, quantum chemical calculations using the "nudged elastic band" concept were employed to estimate activation energies for individual jump processes which in turn could help to identify the bottlenecks in Li mobility. Simulations in former studies[19,20] for pure $Li_4P_2S_6$ suggested that the lithium

Table 2 Comparison of the activation energies for the Li ion mobility obtained from EIS E_A^{EIS} and from NMR E_A^{NMR} and ionic conductivities of $Li_4P_2S_6$ and $Li_{3.74}Mg_{0.13}P_2S_6$ at room temperature $\sigma_{298\ K}$, as well as the effective capacitances $C_{eff,\ 324\ K}$

	$Li_4P_2S_6$	$Li_{3.74}Mg_{0.13}P_2S_6$	$Li_4P_2S_6$, literature
$\sigma_{298\ K}$/S cm^{-1}	$1.5(6) \times 10^{-12}$	$5(1) \times 10^{-11}$	1.6×10^{-10} (ref. 20) 4.7×10^{-5} (ref. 25) 2.4×10^{-7} (ref. 19)
$C_{eff,\ 324\ K}$/pF	59.6(5)	56.2(6)	
E_A^{EIS}/eV	0.86(2)	0.72(1)	
E_A^{NMR}/eV	0.62(6)	0.55(5)	0.48,[20] 0.39,[25] 0.29[19]

ion motion mainly relies on interstitial transport in the x–y-plane of the crystal structure with the space group $P\bar{3}1\,m$, while Li ion diffusion in the z-direction is energetically unfavourable since it involves Li ion jumps between the $P_2S_6^{4-}$ layers. In order to determine the diffusion pathways for $Li_4P_2S_6$ in the space group $P321$, Climbing Image-Nudged Elastic Band (CI-NEB) calculations were carried out.

For the structure in the space group $P321$, potential migration pathways for vacancy mediated diffusion were identified and the activation energies for the local jumps were calculated (Fig. 10).

Migration routes which can contribute to macroscopic Li transport need to cover a complete unit cell. By the simulations it is found that the maximum activation energy which

forms the bottleneck for a migration pathway along the c-axis with 0.52 eV (Fig. S8†) is lower than the corresponding one for a pathway along the a-axis with 0.57 eV (Fig. 10). Both pathways involve more than one elementary hopping process. Certain direct jumps over the center of the void along the P–P axis are penalized by a high activation energy of >1.0 eV (Fig. S9†). It can be concluded that the pathway along the c-axis is preferential and that the Li mobility in $Li_4P_2S_6$ is slightly anisotropic. The value found by the NEB calculations is in good agreement with the values found by impedance spectroscopy. The NEB simulations indicate only a minor distortion of the P_2S_6 group in the transition state which indicates that the potential rotation of the PS_3-unit around the P–P bond is decoupled from the Li-motion. The mobility of the Mg^{2+} ion involves a significantly higher activation energy according to NEB calculations than that of the Li^+ ion between the same two sites (Fig. S7†), i.e. 1.0 vs. 0.52 eV, respectively. This finding is in agreement with the higher formal charge of the Mg^{2+} ion and means that the Mg^{2+} substitution sites need to be circumvented by the mobile Li^+ ions for macroscopic transport.

Conclusions

While aliovalent Mg substitution in $Li_4P_2S_6$ showed a moderate increase in Li ion conductivity, the overall improvement was disappointing. The results indicate that among the factors which explain this observation are the blocking of Li pathways by Mg ions and maybe even more important changes in the crystal structure which can occur even at a low substitution level. For this study it proved beneficial to be able to compare the activation energies for ionic motion from different sources, i.e. impedance spectroscopy, NMR and Nudged Elastic Band calculations.

Author contributions

Conceptualization: JSADG; investigation: SN, NM, SCA; writing – original draft; SN, NM, SCA; writing – review and editing: JSADG; visualization: SN, NM, SCA; funding acquisition: JSADG; supervision: JSADG.

Conflicts of interest

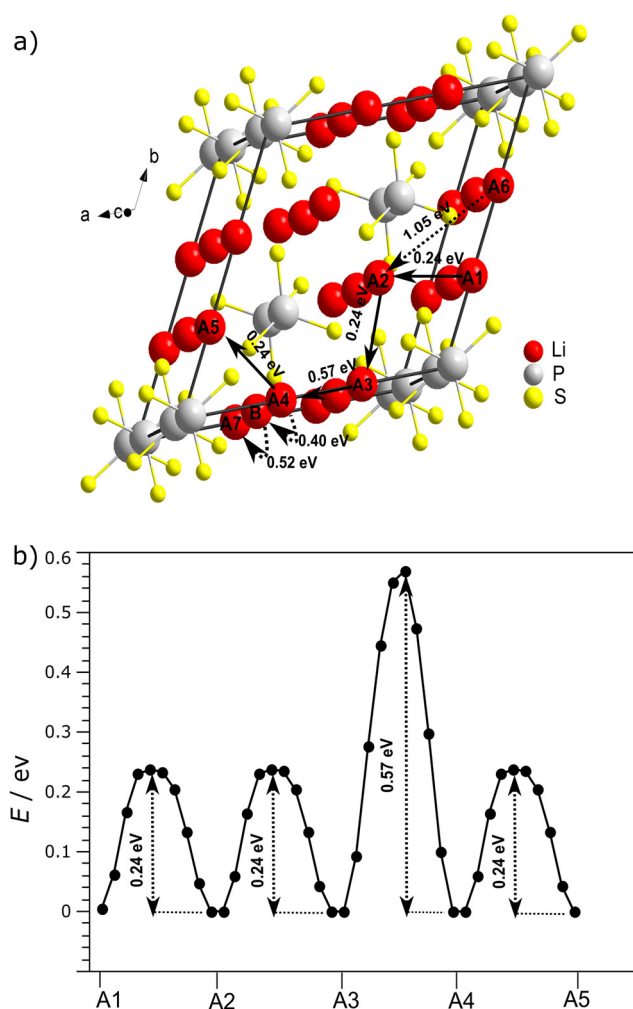There are no conflicts to declare.

Acknowledgements

Fig. 10 Potential pathways of vacancy-based Li migration and the associated activation energies determined from Nudged Elastic Band calculations. (a) Li-ion transport routes along the a-axis A1 → A2 → A3 → A4 → A5 and along the c-axis A4 → B → A7 within the structure of $Li_4P_2S_6$ (space group $P321$). The solid arrows represent the most favorable long-range Li diffusion pathway in the sense of featuring the lowest maximum activation energy. (b) The graph shows the energy barriers along the most favorable pathway along the a-axis for transport over a complete unit cell.

References

1 S. Hama, T. Otomo and K. Kawamoto, JP2014035865(A), 2014.

2 P. Knauth, *Solid State Ionics*, 2009, **180**, 911–916.

3 H.-J. Deiseroth, S.-T. Kong, H. Eckert, J. Vannahme, C. Reiner, T. Zaiß and M. Schlosser, *Angew. Chem., Int. Ed.*, 2008, **47**, 755–758.

4 N. Kamaya, K. Homma, Y. Yamakawa, M. Hirayama, R. Kanno, M. Yonemura, T. Kamiyama, Y. Kato, S. Hama, K. Kawamoto and A. Mitsui, *Nat. Mater.*, 2011, **10**, 682.

5 H. Yang and N. Wu, *Energy Sci. Eng.*, 2022, **10**, 1643–1671.

6 J. Frenkel, *Z. Phys.*, 1926, **35**, 652–669.

7 W. E. Wallace and R. A. Flinn, *Nature*, 1953, **172**, 681–682.

8 A. R. West, *Chem. Rec.*, 2006, **6**, 206–216.

9 T. Famprikis, P. Canepa, J. A. Dawson, M. S. Islam and C. Masquelier, *Nat. Mater.*, 2019, **18**, 1278–1291.

10 L. Zhou, N. Minafra, W. G. Zeier and L. F. Nazar, *Acc. Chem. Res.*, 2021, **54**, 2717–2728.

11 P. Adeli, J. D. Bazak, K. H. Park, I. Kochetkov, A. Huq, G. R. Goward and L. F. Nazar, *Angew. Chem., Int. Ed.*, 2019, **58**, 8681–8686.

12 P. Bron, S. Johansson, K. Zick, J. Schmedt auf der Günne, S. Dehnen and B. Roling, *J. Am. Chem. Soc.*, 2013, **135**, 15694–15697.

13 J. M. Whiteley, J. H. Woo, E. Hu, K.-W. Nam and S.-H. Lee, *J. Electrochem. Soc.*, 2014, **161**, A1812.

14 P. Jakes, J. Granwehr, H. Kungl and R.-A. Eichel, *Z. Phys. Chem.*, 2015, **229**, 1439–1450.

15 P. Adeli, J. D. Bazak, A. Huq, G. R. Goward and L. F. Nazar, *Chem. Mater.*, 2021, **33**, 146–157.

16 H. Schneider, S. J. Sedlmaier, H. Du, T. Kelley, K. Leitner, J. ter Maat, C. Scordilis-Kelley, A. Mudalige, J. Kulisch and L. Schneider, *ChemistrySelect*, 2019, **4**, 3351–3354.

17 Z. Zhang, J. Zhang, H. Jia, L. Peng, T. An and J. Xie, *J. Power Sources*, 2020, **450**, 227601.

18 M. S. Whittingham, Y. Song, S. Lutta, P. Y. Zavalij and N. A. Chernova, *J. Mater. Chem.*, 2005, **15**, 3362–3379.

19 Z. D. Hood, C. Kates, M. Kirkham, S. Adhikari, C. Liang and N. A. W. Holzwarth, *Solid State Ionics*, 2016, **284**, 61–70.

20 C. Dietrich, M. Sadowski, S. Sicolo, D. A. Weber, S. J. Sedlmaier, K. S. Weldert, S. Indris, K. Albe, J. Janek and W. G. Zeier, *Chem. Mater.*, 2016, **28**, 8764–8773.

21 S. Neuberger, S. P. Culver, H. Eckert, W. G. Zeier and J. Schmedt auf der Günne, *Dalton Trans.*, 2018, **47**, 11691–11695.

22 R. Mercier, J. P. Malugani, B. Fahys, J. Douglande and G. Robert, *J. Solid State Chem.*, 1982, **43**, 151–162.

23 A. R. Stamminger, B. Ziebarth, M. Mrovec, T. Hammerschmidt and R. Drautz, *RSC Adv.*, 2020, **10**, 10715–10722.

24 H. Ben Yahia, K. Motohashi, S. Mori, A. Sakuda and A. Hayashi, *Z. Kristallogr. - Cryst. Mater.*, 2023, **238**, 209–216.

25 H. Nagata and J. Akimoto, *ChemistrySelect*, 2020, **5**, 9926–9931.

26 K. Takada, T. Inada, A. Kajiyama, H. Sasaki, S. Kondo, M. Watanabe and M. Kanda, *Solid State Ionics*, 2002, **147**, 23–27.

27 W. Klingen, G. Eulenberger and H. Hahn, *Naturwissenschaften*, 1968, **55**, 229–230.

28 R. K. Harris, E. D. Becker, de M. S. M. Cabral, P. Granger, R. E. Hoffman and K. W. Zilm, *Pure Appl. Chem.*, 2008, **80**, 59–84.

29 R. K. Harris and E. D. Becker, *J. Magn. Reson.*, 2002, **156**, 323–326.

30 D. Jardón-Álvarez and J. Schmedt auf der Günne, *Solid State Nucl. Magn. Reson.*, 2018, **94**, 26–30.

31 A. A. Coelho, *TOPAS-Academic V7.1 (version V7.18) Coelho Software*, Brisbane, 2020.

32 *The Rietveld Method*, ed. R. A. Young, Oxford University Press, Oxford, New York, 1995.

33 P. Virtanen, R. Gommers, T. E. Oliphant, M. Haberland, T. Reddy, D. Cournapeau, E. Burovski, P. Peterson, W. Weckesser, J. Bright, S. J. van der Walt, M. Brett, J. Wilson, K. J. Millman, N. Mayorov, A. R. J. Nelson, E. Jones, R. Kern, E. Larson, C. J. Carey, İ. Polat, Y. Feng, E. W. Moore, J. VanderPlas, D. Laxalde, J. Perktold, R. Cimrman, I. Henriksen, E. A. Quintero, C. R. Harris, A. M. Archibald, A. H. Ribeiro, F. Pedregosa and P. van Mulbregt, *Nat. Methods*, 2020, **17**, 261–272.

34 P. Giannozzi, O. Baseggio, P. Bonfà, D. Brunato, R. Car, I. Carnimeo, C. Cavazzoni, S. de Gironcoli, P. Delugas, F. Ferrari Ruffino, A. Ferretti, N. Marzari, I. Timrov, A. Urru and S. Baroni, *J. Chem. Phys.*, 2020, **152**, 154105.

35 T. Björkman, *Comput. Phys. Commun.*, 2011, **182**, 1183–1186.

36 K. F. Garrity, J. W. Bennett, K. M. Rabe and D. Vanderbilt, *Comput. Mater. Sci.*, 2014, **81**, 446–452.

37 H. J. Monkhorst and J. D. Pack, *Phys. Rev. B: Solid State*, 1976, **13**, 5188–5192.

38 P. E. Blöchl, *Phys. Rev. B: Condens. Matter Mater. Phys.*, 1994, **50**, 17953–17979.

39 G. Henkelman, B. P. Uberuaga and H. Jónsson, *J. Chem. Phys.*, 2000, **113**, 9901–9904.

40 G. Xu, K. Zhong, J.-M. Zhang and Z. Huang, *Solid State Ionics*, 2015, **281**, 1–5.

41 N. Kuganathan, A. L. Solovjov, R. V. Vovk and A. Chroneos, *Heliyon*, 2021, **7**, e07460.

42 S. Jörgens and A. Mewis, *Z. Anorg. Allg. Chem.*, 2004, **630**, 51–57.

43 J. S. Waugh and E. I. Fedin, *Fiz. Tverd. Tela*, 1962, **4**, 2233–2237.

44 J. S. Waugh and E. I. Fedin, *Phys. Solid State*, 1963, **4**, 1633–1636.

45 R. Bertermann and W. Müller-Warmuth, *Z. Naturforsch., A*, 1998, **53**, 863–873.

46 N. Bloembergen, E. M. Purcell and R. V. Pound, *Phys. Rev.*, 1948, **73**, 679–712.